ACS APPLIED MATERIALS & INTERFACES

Research Article

Cite This: ACS Appl. Mater. Interfaces 2018, 10, 42513−42523

www.acsami.org

Evidence for Fast Lithium-Ion Diffusion and Charge-Transfer Reactions in Amorphous TiO_x Nanotubes: Insights for High-Rate Electrochemical Energy Storage

Yu Jiang,*,† Charles Hall,† Ning Song,† Derwin Lau,† Patrick A. Burr,‡ Robert Patterson,† Da-Wei Wang,§ Zi Ouyang,† and Alison Lennon*,†

†School of Photovoltaic and Renewable Energy Engineering, ‡School of Electrical Engineering and Telecommunication, and §Particles and Catalysis Research Group, School of Chemical Engineering, UNSW Sydney, Sydney, NSW 2052, Australia

Supporting Information

ABSTRACT: The charge-storage kinetics of amorphous TiO_x nanotube electrodes formed by anodizing three-dimensional porous Ti scaffolds are reported. The resultant electrodes demonstrated not only superior storage capacities and rate capability to anatase TiO_x nanotube electrodes but also improved areal capacities (324 μAh cm^{-2} at 50 μA cm^{-2} and 182 μAh cm^{-2} at 5 mA cm^{-2}) and cycling stability (over 2000 cycles) over previously reported TiO_x nanotube electrodes using planar current collectors. Amorphous TiO_x exhibits very different electrochemical storage behavior from its anatase counterpart as the majority of its storage capacity can be attributed to capacitive-like processes with more than 74 and 95% relative contributions being attained at 0.05 and 1 mV s^{-1}, respectively. The kinetic analysis revealed that the insertion/extraction process of Li^+ in amorphous TiO_x is significantly faster than in anatase structure and controlled by both solid-state diffusion and interfacial charge-transfer kinetics. It is concluded that the large capacitive contribution in amorphous TiO_x originates from its highly defective and loosely packed structure and lack of long-range ordering, which facilitate not only a significantly faster Li^+ diffusion process (diffusion coefficients of 2×10^{-14} to 3×10^{-13} cm^2 s^{-1}) but also more facile interfacial charge-transfer kinetics than anatase TiO_x.

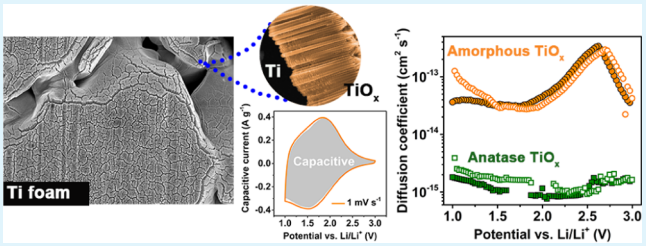

KEYWORDS: *high-rate energy storage, lithium-ion battery, anode material, amorphous TiO_2 nanotubes, insertion kinetics, potentiostatic intermittent titration technique, lithium-ion diffusion*

1. INTRODUCTION

High rate capability is becoming increasingly important for electrochemical energy storage required for electric vehicles and renewable power systems.[1−3] Lithium-ion batteries are considered as the most promising candidates for these applications because of their high energy densities, relatively long cycle lives, and technological maturity in the field of portable electronic devices.[4,5] Yet, challenges remain for them to retain a sufficient energy density, cycle life, and most importantly safe operation when they are charged/discharged at high rates. Enhancing the rate capability of electrode materials requires an understanding of the fundamental processes involved in charging and discharging so that rate-limiting steps can be addressed by systematic engineering. This investigation process is somewhat different from that typically adopted for the objective of increasing energy density, or capacity, where the more common approach is to seek new materials or material combinations that can achieve greater charge storage without significantly impacting cyclability.[6]

Among many anode materials, titanium oxide (TiO_x) has demonstrated attractive features in terms of low cost, minimal solid electrolyte interphase formation and superior coulombic efficiencies and cycling stability[7] due to its excellent structural stability upon lithiation and delithiation with a limited volume change of <4%.[8] More importantly, its high operating potential (ca. 1.5−1.7 V vs Li/Li$^+$) is well above the Li plating potential, making it a safer alternative to the state-of-the-art graphite electrode (lithiation potential at ∼0.1 V vs Li/Li$^+$).[5,7] This characteristic is especially important for high-power devices since Li plating is more likely to occur at high charging/discharging rates.[9] In spite of all of the advantages, bulk TiO_x suffers from the poor ionic and electronic conductivity.[10,11] To overcome these limitations, many studies have reported the use of nanostructured TiO_x (e.g., nanoparticles, nanotubes, nanowires, and mesoporous structures)[7,12] or TiO_x-based composites[13−15] to achieve improved storage capacities and rate capabilities. In particular, self-supported and electrochemically grown TiO_x nanotube (NT) electrodes have drawn significant attention because of their fabrication simplicity, large electrode/electrolyte surface area, short Li^+ diffusion path through the tube walls, and minimal structural changes during cycling.

Received: September 28, 2018
Accepted: November 21, 2018
Published: November 21, 2018

Downloaded via UNIV OF NEW SOUTH WALES on January 8, 2019 at 01:24:06 (UTC).
See https://pubs.acs.org/sharingguidelines for options on how to legitimately share published articles.

 © 2018 American Chemical Society

DOI: 10.1021/acsami.8b16994
ACS Appl. Mater. Interfaces 2018, 10, 42513−42523

The electrochemical performance (capacity, rate capability, and cyclability) and charge-storage mechanisms have been comprehensively studied for crystalline (anatase) TiO_x (hereafter denoted as c-TiO_x) NT electrodes, and results suggest that a considerable fraction of the overall capacity in c-TiO_x NTs arises from capacitive storage processes.[16,17] Interestingly, several recent studies have found that amorphous TiO_x (hereafter denoted as a-TiO_x) electrodes can achieve significantly higher capacities and rate capability than their crystalline counterparts.[18−20] Despite these reports of enhanced performance, investigations on the origin of the enhanced rate in a-TiO_x are limited. Xiong et al.[21] identified capacitive processes for Li^+ storage in a-TiO_x using estimates of *b*-value[22,23] obtained from cyclic voltammetry (CV) measurements. In a later article, the authors attributed the superior capacity and cyclability of a-TiO_x electrodes to the possible atomic rearrangement in the amorphous material when discharged below ∼1 V during the first cycle.[24] Although a detailed microscopic analysis was reported, the discussion on charge-storage kinetics in a-TiO_x was limited to the simulation results. Han et al. further analyzed the diffusive and capacitive contributions of Li^+ insertion in a-TiO_x composite electrodes consisting of thin-film TiO_x and graphene.[25] Despite the outstanding capacity and rate capability of 122 mAh g^{-1} at 100 C being attained by the composite electrodes, the inclusion of graphene (an electric double-layer (EDL) capacitor material) can introduce uncertainties into the analysis of storage mechanism.

In this paper, we have extended the kinetic analyses that have been previously reported for a-TiO_x NT electrode and presented a more detailed investigation of the charge-storage kinetics in both a-TiO_x and c-TiO_x NT electrodes using a combination of electrochemical methods including scan-rate-dependent CV, potentiostatic intermittent titration technique (PITT), and electrochemical impedance spectroscopy (EIS) measurements. From this analysis, we obtained quantitative evidence to elucidate the distinct Li^+-storage behavior and therefore the superior rate performance of a-TiO_x compared to the crystalline form. The NT electrodes were fabricated by electrochemically growing TiO_x NTs on the surface of three-dimensional (3D) porous Ti foams, the foams being utilized as current-collecting scaffolds. The self-supported structure of TiO_x NTs on the foam eliminates the need for any binder or conductive additives, making the electrode an ideal system with which to study the active material's fundamental electrochemical behavior. This study also highlights the potential advantages of using amorphous electrode materials for high-rate electrochemical storage and the need to increase the understanding of Li^+ diffusion and charge-transfer reaction kinetics for these materials.

2. EXPERIMENTAL SECTION

2.1. X-ray Computed Tomography. The 3D micro X-ray computed tomography (CT) was performed using an 8 mm diameter disk of the Ti foam (TOB New Energy) to determine: (i) the open surface area, which is accessible to the electrolyte during anodization, and (ii) the pore size distribution of the foam. The CT images were acquired using a customized CT equipment (Tyree X-ray CT facility, UNSW) with an excitation energy of 120 kV. A steel filter with a thickness of 3 mm was applied to remove the beam hardening and increase the signal contrast.

For quantitative analysis, the reconstructed 3D tomogram was used to determine the different phase materials by a semiautomatic segmentation approach.[26] After segmentation, Ti metal and pores were distinguished and the material defined image was then used to perform the surface density calculation. The open surface area was estimated through surface triangulation on the voxels neighboring Ti metal, and the percolation-type spanning cluster algorithm[27] was employed to bound the calculations only to interconnected and thus accessible pore spaces. Uncertainties in the surface area estimation arose from the noise-to-signal boundary set for the segmentation procedure, the tomogram resolution (i.e, the number of voxels), and the discretization effects.[28] For the analysis in this study, we used tomograms with a 3D of 2520 × 2520 × 1320 voxels (at 4.59 μm voxel size). For the calculations of pore radius distribution, covering radius transform,[27] a method restricted to local pore morphology without considering the history of pore channels (e.g., throats), was performed and the pore size was estimated from the radius of the largest covering sphere in each voxel. Additional figures and details are provided in Supporting Information Figure S1.

2.2. Electrode Preparation. Titania NTs were grown electrochemically by a one-step anodization process. Prior to anodization, pure Ti foams were cleaned by ultrasonication in acetone, isopropyl alcohol, and deionized water for 10 min each. Titanium foams were immersed in the anodization electrolyte (0.45 M NH_4F and 2.5% v/v deionized water in glycerol) and placed in a vacuum environment for 40 min before anodization to ensure the access of electrolyte to the inner surface of the foams. Anodization was performed in a two-electrode configuration with the Ti foam serving as the anode and a platinized Ti plate being used as the cathode. The NTs were grown by applying a constant voltage of 35 V to the Ti foam for 50 min after a voltage ramp of 1 V s^{-1}. After anodization, the Ti foams were first rinsed with deionized water, then soaked sequentially in the mixture of 1:4, 2:3, 4:1 v/v ethanol/deionized water and pure ethanol for 5 min each, and finally dried in ambient air. To prepare crystalline electrodes, the as-anodized TiO_x NTs electrodes were annealed at 400 °C for 1 h in air.

2.3. Material Characterization. Ex situ thin-film X-ray diffraction (XRD) was recorded in a PANalytical Empyrean diffractometer with Cu Kα emission (λ = 1.5418 Å). Raman spectroscopy was acquired using a Renishaw inVia spectrometer with a laser wavelength of 532 nm. Scanning electron microscopy (SEM) and transmission electron microscopy (TEM) were conducted by an FEI Nova NanoSEM 450 FE-SEM microscope and a Phillips CM200 TEM microscope, respectively. Selected area electron diffraction (SAED) pattern was acquired by an FEI Tecnai G2 20 TEM microscope with an aperture diameter of ∼200 nm. X-ray photoelectron spectroscopy (XPS) was conducted by Thermo Scientific UK ESCALAB250Xi under ultrahigh vacuum. The X-ray source was monochromated Al Kα (energy of 1486.68 eV) with the binding energy scale being calibrated using a carbon reference (C 1s = 284.8 eV).

2.4. Electrochemical Characterization. Electrochemical measurements were performed using R2032-type coin cells with TiO_x NTs electrodes serving as the anode and Li foils serving as the cathode. Prior to cell assembly, the as-anodized Ti foams were dried in vacuum at 60 °C for 24 h to remove any residual solvent. A volume of 80 μL of 1 M $LiPF_6$ in a 1:1 v/v mixture of ethylene carbonate and ethyl methyl carbonate was used as electrolyte and battery-grade microporous membranes as separators. All coin cells were assembled in an Ar-filled glovebox and then characterized using an IviumStat.XR potentiostat (Ivium Technologies) in atmosphere at room temperature.

Galvanostatic charge and discharge (GCD) measurements were conducted at different current densities for a potential range of 1.0−3.0 V with respect to the Li/Li^+ potential. These data were used to estimate the areal and specific capacity of TiO_x NTs electrodes. The mass of the active material was estimated from the volume of TiO_x NTs calculated using the SEM images and CT data and by assuming densities of 3.77 and 3.84 g cm^{-3} for the amorphous and anatase TiO_x, respectively.[29] CV curves were recorded at scan rates ranging from 0.05 to 100 mV s^{-1} for the same potential range as the GCD measurements.

DOI: 10.1021/acsami.8b16994
ACS Appl. Mater. Interfaces 2018, 10, 42513−42523

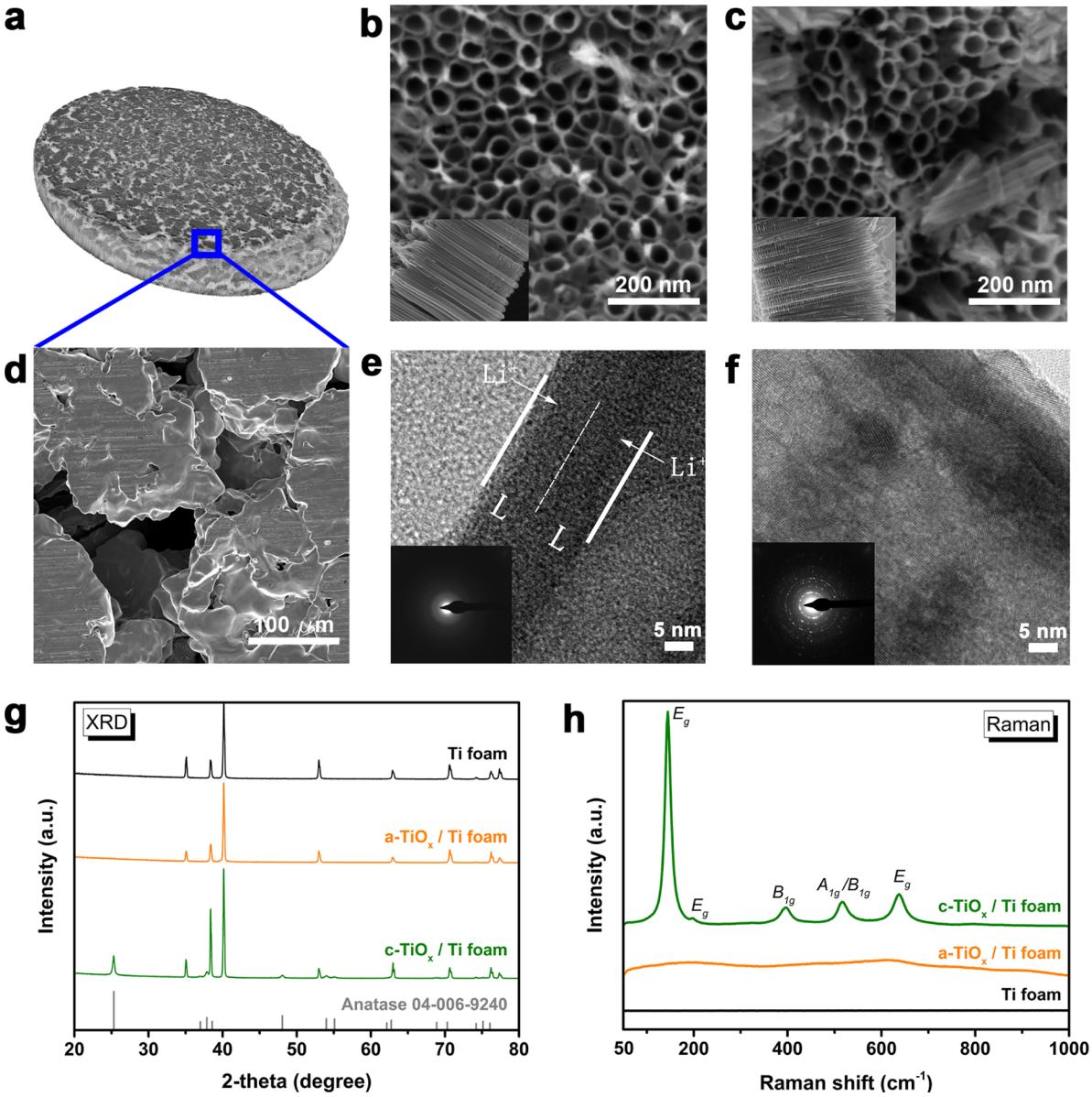

Figure 1. (a) A 3D CT image of a Ti foam before anodization. (b−d) SEM images of a section of as-grown TiO_x NTs, after annealing in air at 400 °C for 1 h, and Ti foam, respectively. The insets in (b) and (c) show cross-sectional SEM images of the TiO_x NTs. (e, f) TEM images of as-grown TiO_x NTs and after annealing in air at 400 °C for 1 h, respectively. The corresponding SAED patterns are shown in the insets of the TEM images (see Supporting Information Figure S2f for further details of SAED patterns). (g, h) XRD patterns and Raman spectra for a Ti foam and TiO_x NTs before and after annealing, respectively.

EIS and PITT measurements[30,31] were performed after 90 CV cycles to ensure quasi-reversible conditions. Prior to EIS measurements, the test cells were discharged to 2 V from their open-circuit voltages to enable comparisons between different cells at the same voltage. The impedance spectra were acquired in a frequency range of 100 kHz to 10 mHz with an AC voltage amplitude of 10 mV. For PITT measurements, the working electrode was first set to 3 V and equilibrated for 500 s. This was followed by the application of a series of potential steps of −25 mV with 500 s equilibration time at each step until the working electrode potential reached the lower limit of 1 V. This process was reversed with a series of potential steps of +25 mV until the potential upper limit of 3 V was reached. The current response after each potential step was recorded with a data collection time step of 0.01 s.

2.5. Scan-Rate-Dependent CV and PITT Analysis. To distinguish quantitatively different storage mechanisms to the overall charge storage in TiO_x electrodes, the current response $I(V)$ at a fixed potential was assumed to be a combination of capacitive (i.e., non-diffusion-controlled) $k_1\nu$ and diffusion-controlled processes $k_2\nu^{1/2}$ [32]

$$I(V) = k_1\nu + k_2\nu^{1/2} \tag{1}$$

where k_1 and k_2 are adjustable parameters. From the CV data, a graph of $I(V)/\nu^{1/2}$ as a function of $\nu^{1/2}$ was generated at each potential for scan rates between 0.05 and 100 mV s^{-1}. Then, k_1 and k_2 were determined from the slope and intercept of the linear fitting to each plot, respectively.

Specific capacities Q of TiO_x electrodes for the different charge-storage processes were estimated from CV curves at different scan rates by integrating their corresponding current $I(V)$ of the anodic half-cycle

$$Q = \frac{\int_{V_0}^{V_1} I(V)\mathrm{d}V}{\nu m} \tag{2}$$

DOI: 10.1021/acsami.8b16994
ACS Appl. Mater. Interfaces 2018, 10, 42513−42523

Table 1. Geometric Parameters of the Ti Foam and TiO_x NTs

sample	porosity %	accessible surface area (mm^2 per mm^3)			
Ti foam	25.2 ± 1.7	14.6 ± 1.0			
	outer diameter (nm)	wall thickness (nm)	tube length (μm)	estimated mass loading[a] (mg cm^{-2})	surface area (m^2 g^{-1})
a-TiO_x	60.2 ± 3.4	30.3 ± 4.9	2.4 ± 0.1	2.4 ± 0.7	73.1 ± 10.2
c-TiO_x	56.1 ± 8.4	29.7 ± 2.1	2.3 ± 0.2	2.4 ± 1.0	67.9 ± 11.0

[a]Mass loading of TiO_x electrodes was estimated using accessible surface area of a Ti foam from the CT analysis and geometry parameters of TiO_x NTs from SEM images.

where V_0 and V_1 define the voltage range for which current is positive, m is the mass of active electrode material, and ν is the scan rate.

For the determination of the chemical diffusion coefficient of a guest species in a thin-film host material, a linear and restricted (blocking) diffusion model in which the diffusion flux is assumed to be zero at some distance L from the electrolyte/electrode interface was used.[33] Using this model, the transient current response from an electrode to a potential step, $I_d(t)$, is given by[31,33]

$$I_d(t) = 2\frac{\Delta Q}{\tau_d}\sum_{n=1}^{\infty}\exp\left[-(2n-1)^2\frac{\pi^2 t}{4\tau_d}\right] \tag{3}$$

where t is the elapsed time from the start of the potential step. The diffusion time constant τ_d and the amount of faradic charge passed during the process ΔQ are defined by

$$\tau_d = L^2/D,\ \ \Delta Q = \int_0^{\infty} I_d(t)\mathrm{d}t = -FAL\Delta c \tag{4}$$

where L is the diffusion length, D is the chemical diffusion coefficient of guest species, F is the Faraday constant, A is the electrochemically active surface area, and Δc is the change of guest species concentration in the host material due to the applied potential step. This model assumes that the insertion reaction of the guest species in host material is solely governed by a diffusion process (i.e., very fast charge-transfer kinetics with negligible Ohmic potential drop and EDL charging current).

However, as already discussed in a number of reports,[34,35] application of this model to insertion materials, which exhibit slow charge-transfer kinetics and/or non-negligible Ohmic resistance, can result in erroneous estimates for diffusion coefficients. In this study, we employed the model reported by Montella[34] to analyze Li^+ insertion in a-TiO_x and c-TiO_x host materials. This model assumes an insertion process under the mixed control of: (i) linear restricted diffusion; (ii) charge-transfer kinetics at electrode/electrolyte and electrode/current collector interface; and (iii) Ohmic potential drop. Using this model, the current response $I(t)$ to a small potential step can be expressed as

$$I(t) = 2\frac{\Delta Q}{\tau_d}\sum_{n=1}^{\infty}\frac{\Lambda^2}{\Lambda^2+\Lambda+b_n^2}\exp\left(-\frac{b_n^2 t}{\tau_d}\right) \tag{5}$$

where b_n is the nth positive root of the equation

$$b\tan b - \Lambda = 0 \tag{6}$$

The dimensionless parameter Λ provides a measure of the relative contributions of diffusion and other rate-limiting processes

$$\Lambda = \frac{R_d}{R_\Omega + R_{ct}} \tag{7}$$

where R_d is the diffusion resistance, R_Ω is the Ohmic resistance, and R_{ct} is the interfacial charge-transfer resistance. It should be noted that this kinetic model also assumes that the contribution of EDL charging current is small compared to the total current. The validity of this assumption is discussed further in the Results and Discussion section.

After each potential step, the current transient $I(t)$ was recorded and eq 5 was fitted to the data using nonlinear least-squares regression, with Λ, τ_d, and ΔQ being treated as fitting parameters. To ensure fair contributions from data in different time domains, the measured data were interpolated to a fixed number of equidistant points on a log(t) scale and this data set was used for the curve fitting procedure.[35] The initial guess of ΔQ was estimated from the integral of current transient $I(t)$ with respect to t. The summation term in eq 5 was iterated until the nth term was less than 10^{-6} of the sum of previous terms. Given that Li^+ diffusion in the electrolyte is typically orders of magnitude faster than in solid-state host materials[36,37] and the specific capacities of TiO_x NT electrodes have been found to be independent of the tube length (at least for tube length <3.8 μm),[16] it was assumed that transport of Li^+ into the inner- and internanotube voids readily occurs and Li^+ insertion/extraction can occur homogeneously across the entire length of a nanotube and symmetrically from both sides of the tube wall. Therefore, in the calculations of Li^+ diffusion coefficients in host TiO_x NTs, symmetrical linear diffusion was assumed, and the diffusion length L in eq 4 was assumed to be 1/2 of the wall thickness of TiO_x NTs (Figure 1e). The goodness of fit was evaluated using an R-square analysis, and additional details are provided in Supporting Information Figure S5.

3. RESULTS AND DISCUSSION

The 3D porous Ti foam scaffolds provided an interconnected metallic network for electron transport while also facilitating electrolyte access to the inner and outer surfaces of the foam (Figure 1a,d). The open surface area (i.e., surface area accessible to electrolyte) and porosity of the foams used were computed to be 14.6 mm^2 per mm^3 and ~25%, respectively, from the X-ray CT analysis. Approximately 83% of the pores were estimated to have an equivalent radius between 25 and 100 μm, ~16% to have a radius <25 μm and ~1% to have a radius >100 μm (see Figure S1d). Self-supported TiO_x NTs were grown on both the outer and inner surfaces of the foams during the anodization process (Figure S2). The rough initial surface of the Ti foam provided for strong adhesion of the self-supported TiO_x NTs to the Ti surface and therefore good electrical contact between the TiO_x and the Ti of the scaffold. This eliminated the need for any binders and conductive additives.

The as-grown TiO_x NTs had an average outer diameter of 60.2 ± 3.4 nm and a tube length of 2.4 ± 0.1 μm, as shown in Figure 1b and Table 1. Assuming the geometry of TiO_x NTs shown in the SEM images and a homogeneous cover of TiO_x NTs on the entire open surface area of the Ti foam, the specific surface area was estimated to be 73.1 m^2 g^{-1}. This represents a significant increase over the specific surface area of TiO_x NTs grown on planar Ti foils (24−28 m^2 g^{-1} [38] and 38−47 m^2 g^{-1} [39,40]). A mass loading of 2.4 mg cm^{-2} (per electrode projection area) was calculated for the TiO_x film thickness (i.e., NT length) of 2.4 μm. The TEM image of an NT before annealing (Figure 1e) showed no lattice fringes, and the SAED (Figure 1e inset) was featureless, indicating that the as-grown TiO_x NTs were amorphous (at least long order of lattice structure was absent), which is in agreement with previous reports.[19,41] The XRD spectrum (Figure 1g) confirmed the

DOI: 10.1021/acsami.8b16994
ACS Appl. Mater. Interfaces 2018, 10, 42513−42523

amorphous form of the as-grown TiO_x NTs (so hereafter denoted as a-TiO_x) with the only evident peaks corresponding to Ti metal. The Raman spectrum (Figure 1h) of a-TiO_x showed very weak and broad peaks (distinct from the flat line for the Ti foam) suggesting the presence of some short-range local ordering in the a-TiO_x.[25] After annealing, no significant changes in the morphology of TiO_x NTs were observed (Figure 1c); however, lattice fringes were evident in the TEM image in Figure 1f and the SAED diffraction rings (Figure 1f, inset) corresponded to the *d*-spacing of polycrystalline anatase TiO_2 (*I*41/*amd*). The anatase phase of the annealed TiO_x NTs was also confirmed by XRD patterns (Figure 1g) and Raman spectra (Figure 1h), so hereafter we denote this electrode as c-TiO_x. Chemical composition of TiO_x NTs was investigated using XPS. The measured Ti 2p core-level spectra of a-TiO_x and c-TiO_x (Figure S6a) showed two distinct peaks at binding energies of 464.4 and 458.8 eV, respectively, which are close to the typical values reported for the $2p_{1/2}$ and $2p_{3/2}$ doublet of Ti^{4+}, suggesting that the surface films of both a-TiO_x and c-TiO_x electrodes were stoichiometric TiO_2. However, stoichiometry of the film interiors is difficult to be determined accurately using XPS as the oxidation state of Ti can be affected by sputtering, a process typically used in the depth profiling analysis to etch the film surface.

The a-TiO_x and c-TiO_x electrodes were each combined with a Li foil electrode and assembled into coin cells to assess their electrochemical performance. Figure 2a,b shows the GCD curves of the a-TiO_x and c-TiO_x electrodes for Li^+ insertion/extraction at C-rates between 0.125 C and 12.5 C (the 1 C value was defined as 168 mA g^{-1} corresponding to 1 h charge/discharge current of a theoretical capacity of 168 mAh g^{-1}, which assumes a stoichiometry of 0.5 Li per TiO_2 formula unit[16,23,42]). The c-TiO_x electrode (Figure 2b) exhibited plateaus at ∼1.75 and ∼1.9 V in the lithiation and delithiation curves, respectively. These correspond to a phase transition between the Li-poor Li_xTiO_2 ($0.01 < x \leq 0.21$) with tetragonal anatase structure ($I4_1/amd$) to the orthorhombic Li-titanate ($Li_{\sim 0.55}TiO_2$) phase (*Imma*).[43] The phase transitions are in good agreement with those reported for anatase TiO_x electrodes in the literature.[16,19,29,44] In addition to the main plateaus, an additional pair of plateaus, observed at ∼1.46 V (lithiation) and ∼1.73 V (delithiation), are indicative of a second-phase transition to a fully lithiated Li_1TiO_2 ($I4_1/amd$), which typically occurs in TiO_x crystallites with size <7 nm.[43,45] In contrast, no plateaus were present in the lithiation/delithiation curves of the a-TiO_x electrode and the voltage varied almost linearly with capacity, indicating a capacitive-like storage behavior.[46]

The specific capacities of the a-TiO_x and c-TiO_x electrodes at different C-rates were calculated from the GCD measurements (see Figure 2c). The a-TiO_x electrode demonstrated superior specific capacity and rate capability to the c-TiO_x electrode, achieving ∼135 mAh g^{-1} at 0.125 C (21 mA g^{-1}) and 77 mAh g^{-1} (i.e., 56% capacity retention) at 12.5 C (2106 mA g^{-1}) in contrast to ∼102 mAh g^{-1} at 0.125 C and 28 mAh g^{-1} at 12.5 C (i.e., 27% capacity retention) being attained by the c-TiO_x electrode. Such specific capacities are slightly lower than the previously reported values for electrochemically grown a-TiO_x and c-TiO_x NT electrodes (see Table S1). The slightly lower values may be due to an overestimation of the active material mass (leading to an underestimation of the electrode specific capacities) as the lengths of TiO_x nanotubes grown on the outer surface of a Ti foam were used in the

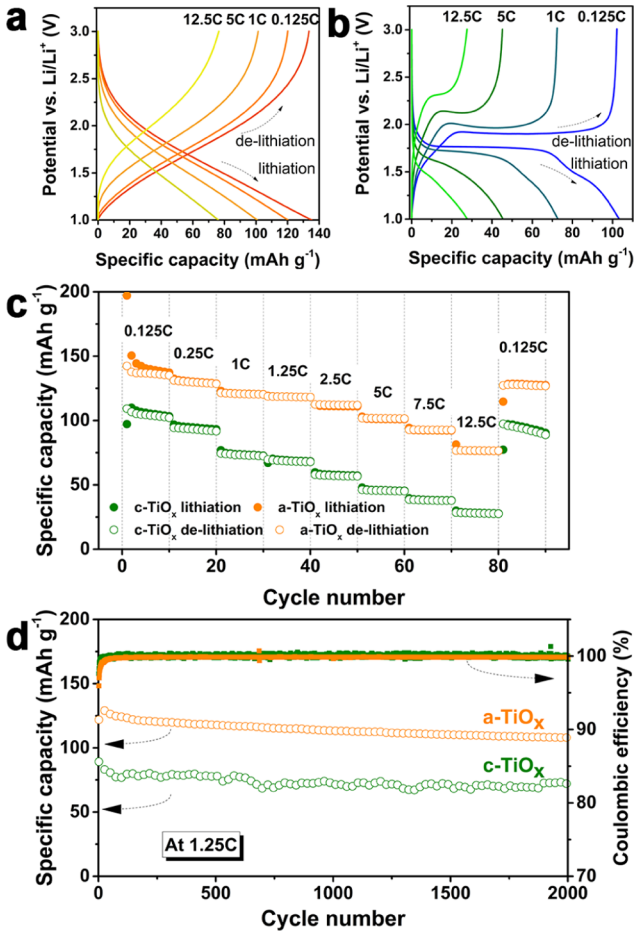

Figure 2. Electrochemical performance of a-TiO_x and c-TiO_x electrodes. GCD profiles of (a) a-TiO_x and (b) c-TiO_x electrodes measured at C-rates between 0.125 and 12.5 C. (c) Rate capability, and (d) cycling stability and coulombic efficiencies of a-TiO_x and c-TiO_x electrodes.

material mass calculation; however, shorter nanotubes were observed on the inner foam surfaces presumably due to a limited access of electrolyte within the deeper pores of the foam during anodization. On the other hand, the areal capacities of the a-TiO_x electrode achieved in this study (calculated using the projection area of the electrode), 324 μAh cm^{-2} at 50 μA cm^{-2} and 182 μAh cm^{-2} at 5 mA cm^{-2}, represent a significant increase over the corresponding previously reported values, 68−200 μAh cm^{-2} at 5−10 μA cm^{-2} and 30−115 μAh cm^{-2} at 0.1−0.5 mA cm^{-2} [39,41,47] (see Supporting Information Figure S3 and Table S2 for details). The improved areal capacities at both low and high rates were presumably due to the large electrode surface area realized by using the 3D porous Ti foams as current-collecting scaffolds. This ensures a larger per-area mass loading of active material (higher areal capacities) without significant increases in the a-TiO_x film thickness, leading to an improved rate capability. The a-TiO_x electrodes demonstrated excellent cycling stability, attaining a capacity retention of 92% (108 mAh g^{-1}) after 2000 cycles and Coulombic efficiencies of 99.9 ± 0.15% in comparison to 80% (71 mAh g^{-1}) and 100 ± 0.29% for the c-TiO_x electrodes (Figure 2d).

Figure 3a,b shows the results of CV measurements between 1 and 3 V vs Li/Li^+ with scan rates ranging from 0.05 to 100 mV s^{-1} for the a-TiO_x and c-TiO_x electrodes, respectively. For

DOI: 10.1021/acsami.8b16994
ACS Appl. Mater. Interfaces 2018, 10, 42513−42523

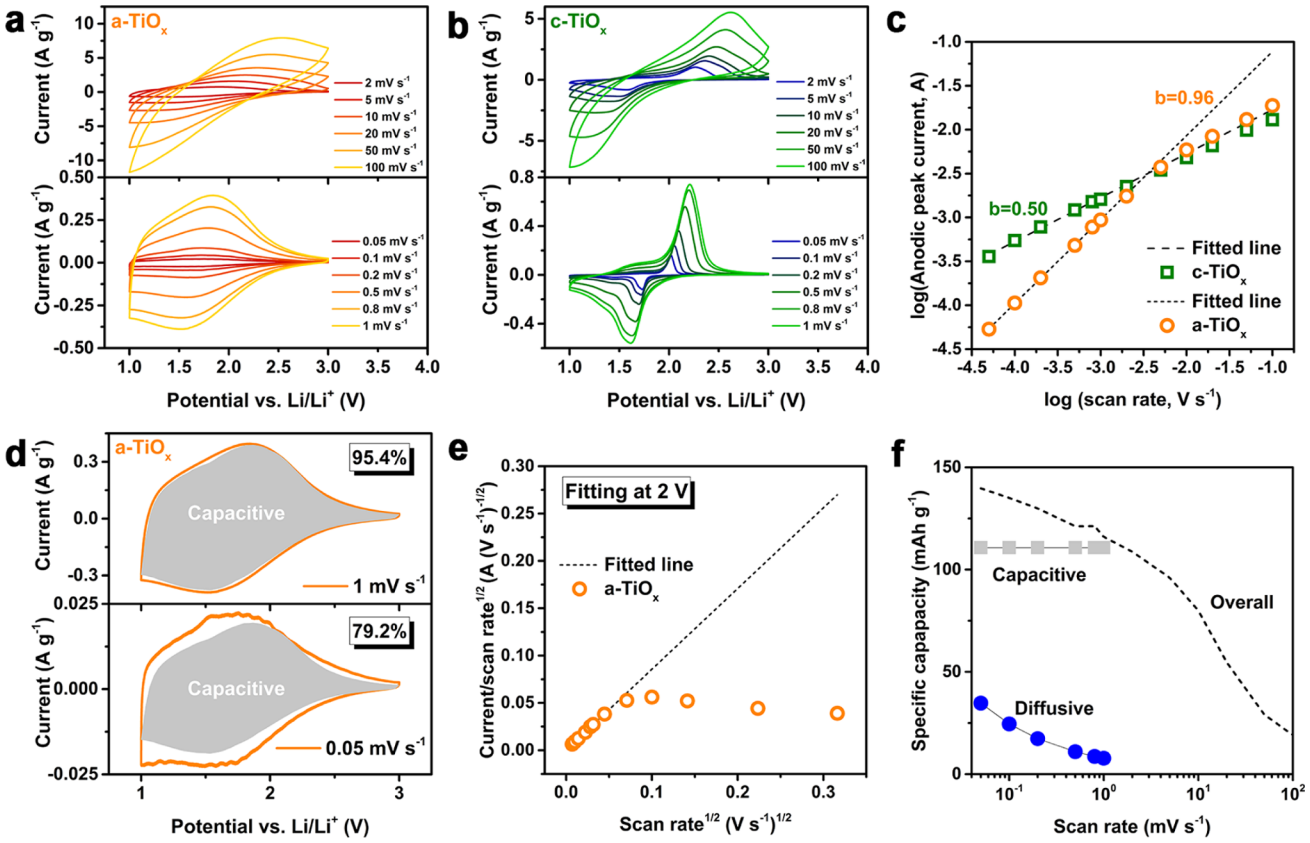

Figure 3. Charge-storage mechanism analysis of the a-TiO_x and c-TiO_x electrodes. CV curves of the (a) a-TiO_x and (b) c-TiO_x electrodes measured at low (bottom) and high (top) scan rates. (c) Determination of the *b*-values, where the dashed lines are linear regression models to fit the experimental data. (d) Separation of the capacitive and diffusion current in the a-TiO_x electrode. (e) Example determination of capacitive and diffusion relative contributions from the slope and intercept of fitted line for the a-TiO_x electrode at a potential of 2 V. (f) Specific capacities of the capacitive and diffusion component for the a-TiO_x electrode at various scan rates.

the c-TiO_x electrode, two pairs of sharp peaks were distinct in the CV curves, i.e., main peaks at 1.73/2.0 V and small peaks at 1.46/1.7 V, which are in good agreement with the plateau positions identified in the GCD curves. Such sharp peaks were absent in the CV curves for the a-TiO_x electrode, and instead, two broad humps over a large range of potentials were evident. This CV response was previously ascribed to the nonuniform distribution of free spaces in the highly disordered and defective structures of the a-TiO_x material, resulting in a broad potential range for Li^+ insertion/extraction.[19,48]

To understand the reasons why a-TiO_x electrodes have improved storage capacities and rate capability than c-TiO_x electrodes, the scan-rate-dependent CV data were analyzed and the *b*-values were determined from the anodic peak current I_p in CV curves at various scan rates ν according to[22,23]

$$I_p = a\nu^b \tag{8}$$

where *a* and *b* are adjustable parameters. Figure 3c depicts the $\log I_p$ vs $\log \nu$ plots for the a-TiO_x and c-TiO_x electrodes and the fitted lines to the measured data, from which the slopes were used to determine the *b*-values for both electrodes. A *b*-value of 0.5 indicates a diffusion-controlled process, whereas a value of 1 implies a capacitive storage process.[22] It worth clarifying that, although termed as "capacitive", the capacitive component in this study is the sum of any non-diffusion-controlled contributions, which includes EDL storage,[49] surface pseudocapacitive storage,[50] and/or bulk-insertion pseudocapacitive storage.[51,52] For scan rates between 0.05 and 2 mV s^{-1}, the *b*-value for the c-TiO_x electrode was estimated to be 0.50, suggesting a diffusion-controlled Li^+ insertion/extraction process in c-TiO_x. In contrast, the a-TiO_x electrode showed a *b*-value of 0.96, indicating that Li^+ storage in its structure was predominantly capacitive. Unfortunately, the $\log I_p$ vs $\log \nu$ plots for both electrodes deviate from the linear model at scan rates >2 mV s^{-1}, making it unreliable to analyze charge-storage mechanisms at higher scan rates.

By employing the approach reported by Liu et al.,[32] the diffusion-controlled and capacitive contributions to the current in CV curves for a-TiO_x electrode were quantitatively separated and are shown in Figure 3d. Results suggest that, in a-TiO_x, the capacitive contribution dominates the overall charge storage over the entire investigation potential range even when cycling at low scan rates of 0.05 and 1 mV s^{-1} (corresponding to 22 and 1 h round-trip cycles). On the basis of these results, specific capacities due to the different charge-storage processes were determined and are shown in Figure 3f. Specific capacities of the capacitive contribution retain their initial values for scan rates of 0.05−1 mV s^{-1}, whereas the values of diffusive contribution decrease rapidly with increasing scan rates as expected. This resulted in a fractional increase of capacitive capacity from 79.2% at 0.05 mV s^{-1} to 95.4% at 1 mV s^{-1} in the a-TiO_x electrode. Considering that the morphology of NTs and therefore the electrode surface area are similar between the a-TiO_x and c-TiO_x electrodes (see Figure 1b,c), differences in their electrochemical storage behavior suggested by the *b*-value analysis cannot be solely

DOI: 10.1021/acsami.8b16994
ACS Appl. Mater. Interfaces 2018, 10, 42513−42523

explained by surface-storage processes (i.e., EDL and surface pseudocapacitive storage). In fact, a recent investigation reported that, in a-TiO_x, a part of this capacitive storage behavior was realized in the bulk material and consequently has been attributed to insertion pseudocapacitive storage.[25] It should be noted that, although analysis using scan-rate-dependent CV has been widely adopted to differentiate the contributions of the different storage mechanisms, linear fitting to the proposed model is not always valid and is often limited to a small scan rate range[23,25,53−55] due to scan-rate-dependent peak shifting and broadening.[56] In our material system (a-TiO_x), as depicted in Figure 3e, linear fitting to the measured data is only possible for low scan rates, restricting the validity of our analysis up to 1 mV s^{-1} (results obtained for c-TiO_x electrode are not physically meaningful due to its apparent peak shifting even in the small scan rate range, see Figure S4).

We used the PITT measurement analysis to elucidate the origin of the high fraction of capacitive storage in a-TiO_x in contrast to its c-TiO_x counterpart. Figure 4a shows the recorded current response of the a-TiO_x electrode after each potential step. As an example, Figure 4b,c depicts in linear and logarithmic scales, respectively, the measured current at the potential of 1.5 V. The solid curves represent the nonlinear least-squares fit to the measurement data using eq 3 (pure diffusion-controlled insertion process; blue curve) and eqs 5 and 6 (mixed-controlled process; orange curve). Assuming a pure diffusion-controlled insertion process clearly overestimated the current response to the potential step in the short-time domain (<∼5 s) and underestimated the response in the long-time domain (>∼50 s). The model deficiency is more clearly illustrated in the logarithmic scale, in which a pure diffusion process should follow the Cottrell relation in the short-time domain with a slope of 0.5.

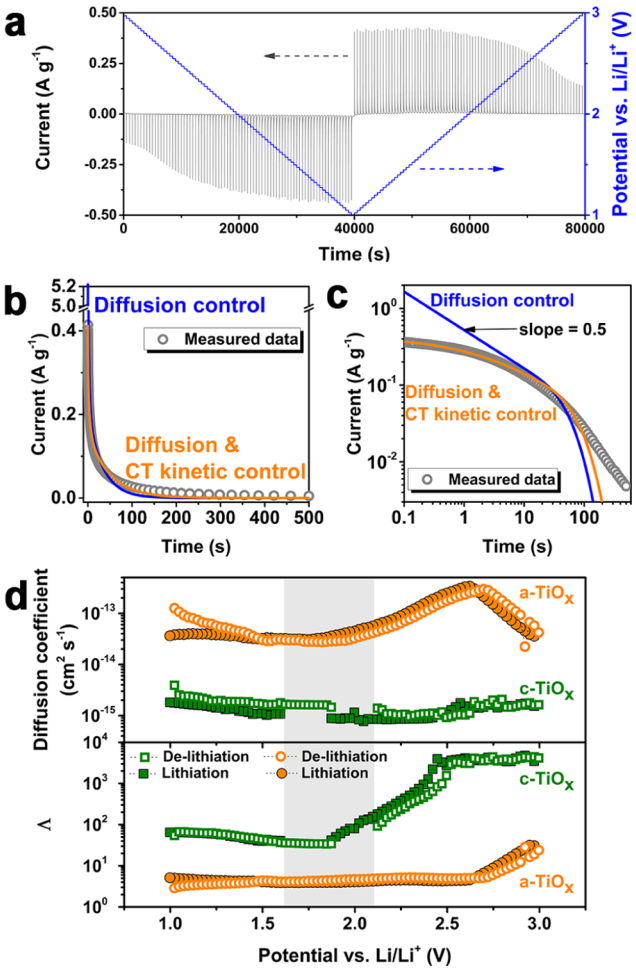

Figure 4. (a) Potential steps and current response profiles of the a-TiO_x electrode during a PITT measurement. (b, c) Measured current response instantly after a potential step from the a-TiO_x electrode at an example potential of 1.5 V and the fitted curves using the restricted diffusion model (blue) and mixed-controlled model (orange) in linear (b) and logarithmic (c) scales. (d) Estimated Li^+ diffusion coefficients and Λ values obtained from the PITT analysis for a-TiO_x and c-TiO_x electrodes.

The measured current is more accurately described by Montella's mixed-controlled model (eqs 5 and 6) in both short- and long-time domains, suggesting that Li^+ insertion/extraction in a-TiO_x is not solely governed by solid-state diffusion in host structures, but rather the interfacial charge-transfer kinetics and Ohmic potential drop also contribute to limiting rate at which charge can be stored.[34] By performing similar curve fitting using eqs 5 and 6 to the current transients after each potential step, the chemical diffusion coefficients D of Li^+ in a-TiO_x and c-TiO_x were determined and are graphed in Figure 4d as a function of potential vs Li/Li^+. It should be noted that current transients measured at potentials at which phase transitions occur in the material (corresponding to CV peak positions) cannot be described adequately by eq 5 and therefore the D values estimated for the c-TiO_x electrode in these regions were omitted (shaded area in Figure 4d). Considering that the surface-area-normalized EDL capacitance was typically in the range of 2−20 μF cm^{-2},[57,58] the estimated surface area of 73.1 m^2 g^{-1} (Table 1) for the a-TiO_x electrode would result in an EDL capacity of 0.8−8.0 mAh g^{-1}, which represented a small proportion to the overall capacity of the a-TiO_x electrode (77−135 mAh g^{-1}). This again proves the validity of the mixed-controlled model, as one assumption made by this model is that the contribution of EDL charging current is small compared to the total current.

The estimated D values for c-TiO_x are in the ranges of 7.7×10^{-16} to 1.8×10^{-15} and 9.2×10^{-16} to 3.9×10^{-15} cm^2 s^{-1} for Li^+ insertion and extraction, respectively. These values are consistent with previously reported values.[23,44,59,60] In contrast, the D values for a-TiO_x are 3.1×10^{-14} to 3.4×10^{-13} cm^2 s^{-1} for Li^+ insertion and 2.2×10^{-14} to 3.0×10^{-13} cm^2 s^{-1} for Li^+ extraction, almost 2 orders of magnitude larger than those for c-TiO_x, implying that Li^+ diffusion in a-TiO_x is significantly faster than in c-TiO_x. This is likely due to crystallographic differences inherent in a-TiO_x and c-TiO_x. The absence of long-range ordering (Figure 1g,h) and the loosely packed structure[61] of a-TiO_x can provide more free space and open spatial channels than available in c-TiO_x (anatase), and therefore enable a facile diffusion pathway of Li^+ in its host structure.

The parameter Λ, defined as the ratio of R_d to the sum of R_Ω and R_{ct} (eq 7), provides a measure of the relative contributions of diffusion and other rate-limiting processes. A large Λ value is characteristic of a diffusion-controlled process, whereas a small Λ value indicates a charge-transfer kinetically limited process and/or non-negligible Ohmic resistance. The large Λ values in the order of ca. 10^2−10^3 for c-TiO_x indicate that solid-state diffusion of Li^+ is the rate-limiting step, which confirms the results suggested by the b-value of 0.50 (see Figure 3c). Except for potentials >2.75 V, the Λ values of 1−10 for a-TiO_x are

DOI: 10.1021/acsami.8b16994
ACS Appl. Mater. Interfaces 2018, 10, 42513−42523

substantially smaller suggesting a mixed-controlled insertion process, provided that the series resistances R_Ω between the two electrodes are comparable as discussed later.

The solid-state diffusion of Li^+ in a-TiO_x is sufficiently fast that its diffusion rate becomes competitive with the rate of charge transfer at the interface. Therefore, in the host structure of a-TiO_x, both processes control the rate of Li^+ insertion/extraction and this explains the high fraction of non-diffusion-controlled contributions in a-TiO_x electrodes. The limiting of the charging/discharging rates of LIBs by the kinetics of charge-transfer reactions has also been observed for (crystalline) $LiFePO_4$, one of the most intensively studied LIB cathode materials, by Bai and Bazant.[62] For $LiFePO_4$, the kinetics of charge storage were able to be remarkably enhanced by carbon coating of the metal oxide to increase electronic conductivity;[62,63] however, many recent reports also highlighted the importance of the minimizing reorganizational energy of the Li^+ at the electrolyte interface and suggested that higher rates may be achieved with 3D semiconducting electrodes.[64] These reports highlight the importance of addressing limitations with regard to the charge-transfer kinetics if high-rate energy storage is to be achieved practically.

To validate the results from the PITT analysis, EIS measurements were performed for each of the a-TiO_x and c-TiO_x electrodes at a potential of 2 V. Figure 5 depicts the

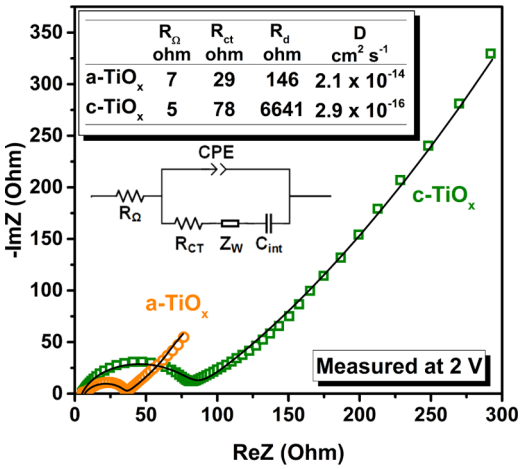

Figure 5. Nyquist plots of the a-TiO_x and c-TiO_x electrodes showing measured data and best fitted curves (solid lines) from equivalent circuit models shown in the inset: R_Ω is the electrolyte resistance, R_{ct} is the interfacial charge-transfer resistance, CPE is a constant phase element modeling the EDL capacitance at the electrode/electrolyte interface, Z_w is the finite-length Warburg element, and C_{int} is the differential intercalation capacitance. Fitted values for the key circuit elements are summarized in the table (see Table S3 for all parameters).

Nyquist plots of both electrodes with symbols representing the measured data and lines showing the best fits by using the equivalent circuit depicted in the inset of Figure 5. In the equivalent circuit, R_Ω is the electrolyte resistance, R_{ct} is the charge-transfer resistance, and a constant phase element (CPE)[65,66] was used to model the EDL capacitance at the electrode/electrolyte interface. The low-frequency data were simulated by the Frumkin and Melik-Gaykazyan impedance,[29,44,67,68] which is equivalent to a finite-length Warburg element, Z_w,[69] in series with a differential intercalation capacitance, C_{int}, representing, respectively, the solid-state diffusion of Li^+ and the accumulation/consumption step of Li^+ in the host material. Modeling impedance spectra using equivalent circuits alone, without adequate understanding of the materials system and structure, can raise the problem of ambiguity. In our analysis, it was noted that multiple combinations of R_d and D values can represent the same set of experimental data. Therefore, we fixed diffusion resistance R_d as an input parameter using the value estimated from the Λ (see eq 7) to determine the diffusion coefficient D. The resulting parameters for the key circuit elements are reported in the table in Figure 5 (see Table S3 for parameters of all circuit elements).

The fitting resulted in D values of 2×10^{-14} and 3×10^{-16} $cm^2\ s^{-1}$ for the a-TiO_x and c-TiO_x electrodes, respectively. These estimates are consistent with the values obtained from the PITT analysis at the same potential (4×10^{-14} $cm^2\ s^{-1}$ for a-TiO_x and 1×10^{-15} $cm^2\ s^{-1}$ for c-TiO_x). Remarkably, although the series resistance R_Ω values were comparable for the two electrodes, the charge-transfer resistance R_{ct} of a-TiO_x (29 Ω) was significantly lower than that of c-TiO_x electrode (78 Ω). This suggests that not only is Li^+ diffusion faster in the a-TiO_x electrode than in the c-TiO_x electrode, but also the interfacial charge transfer may occur more rapidly in the amorphous material further contributing to its superior storage capacities and rate capability than the c-TiO_x electrodes. One possibility is that Li^+ can "enter" the a-TiO_x over the entire surface exposed to the electrolyte while, for c-TiO_x, ions need to diffuse laterally across the crystalline surface before their position coincides with a crystal channel into which the ions can diffuse. The surface of anatase TiO_x is anisotropic, and Li^+ insertion and diffusion is more facile along the [001] direction.[44] Figure 1f suggests that the c-TiO_x NTs were highly polycrystalline in structure with many different grain orientations. This would imply that nonpreferential crystal planes (other than (004)) may be exposed on the NT surface. Kang and Ceder reported enhanced charging/discharging rates for $LiFePO_4$ electrodes by coating crystalline $LiFePO_4$ micrometer-sized particles with an amorphous film.[70] They attributed the higher rate to faster transport of Li^+ to the preferential (010) facets from which they can be inserted in the metal oxide matrix.

4. CONCLUSIONS

The capacity and rate capability of a-TiO_x and c-TiO_x NT electrodes, formed by anodizing porous Ti foam current collectors, were analyzed and compared in this study. The Ti foam provided an interconnected metallic network for electron transport and a large open surface area of 14.6 mm^2 per mm^3, which ensured a high per-area mass loading of the active material without significantly compromising the electrode rate capability. The a-TiO_x/Ti foam electrode demonstrated superior specific capacities (~135 mA g^{-1} at 0.125 C and 77 mA g^{-1} at 12.5 C) and rate capability (56% capacity retention) than its anatase counterpart (27% capacity retention). The achieved areal capacities of 324 μAh cm^{-2} at 50 μA cm^{-2} and 182 μAh cm^{-2} at 5 mA cm^{-2} and excellent cycling stability over 2000 cycles represented a significant improvement over many previously reported TiO_x NTs electrodes utilizing planar foils.

Scan-rate-dependent CV analysis resulted in a b-value of 0.96 for the a-TiO_x electrode and suggested that capacitive contributions dominated its overall storage capacities even at low scan rates (95.4% at 1 mV s^{-1}). The kinetic analysis

DOI: 10.1021/acsami.8b16994
ACS Appl. Mater. Interfaces 2018, 10, 42513−42523

revealed that the diffusion coefficient of Li^+ in the a-TiO_x NT electrode (2×10^{-14} to 3×10^{-13} cm^2 s^{-1}) was almost 2 orders of magnitude larger than that estimated for the c-TiO_x electrode. This faster diffusion of Li^+ resulted in the insertion/extraction of Li^+ in a-TiO_x being more appropriately described by a mixed-controlled process, with the rate not being purely limited by solid-state diffusion. Interestingly, the value of R_{CT} estimated for the a-TiO_x (29 Ω) was also significantly less than that for c-TiO_x (78 Ω), highlighting that not only do the Li^+ diffuse more rapidly in the amorphous material, but the rate of the charge-transfer reaction is also higher. This superior rate capability of a-TiO_x was attributed to its highly defective structure, loose atomic packing, and lack of long-range ordering. This study also highlights the importance of identifying the key rate-limiting processes at an electrode surface if the rate capability of electrode materials is to be enhanced.

■ ASSOCIATED CONTENT

Supporting Information

The Supporting Information is available free of charge on the ACS Publications website at DOI: 10.1021/acsami.8b16994.

> CT tomograms and pore size distribution; additional SEM and TEM images of TiO_x nanotubes/Ti foam; areal rate capability and cycling stability measurements; charge-storage mechanism analysis of c-TiO_x electrodes; *R*-square values for the fitting of PITT data; XPS Ti 2p and O 1s core-level spectra; and electrochemical performance of TiO_x nanotube electrodes previously reported in the literature (PDF)

■ AUTHOR INFORMATION

Corresponding Authors

*E-mail: yu.jiang1@unsw.edu.au (Y.J.).
*E-mail: a.lennon@unsw.edu.au (A.L.).

ORCID

Yu Jiang: 0000-0003-1266-4720
Patrick A. Burr: 0000-0003-4796-9110
Da-Wei Wang: 0000-0002-6651-4261

Notes

The authors declare no competing financial interest.

■ ACKNOWLEDGMENTS

This work was supported by the Australian Research Council through Discovery Grant DP170103219 "Advanced Electrochemical Capacitors". The first author acknowledges the Australian Government Research Program for providing the PhD scholarship. The authors thank Dr. Ji-Youn Arns and Prof. Christoph H. Arns for the acquisition and analysis of the X-ray CT images, and Yicong Hu for the acquisition of TEM images.

■ REFERENCES

(1) Luo, X.; Wang, J.; Dooner, M.; Clarke, J. Overview of Current Development in Electrical Energy Storage Technologies and the Application Potential in Power System Operation. *Appl. Energy* **2015**, *137*, 511−536.

(2) Jiang, Y.; Fletcher, J.; Burr, P.; Hall, C.; Zheng, B.; Wang, D.-W.; Ouyang, Z.; Lennon, A. Suitability of Representative Electrochemical Energy Storage Technologies for Ramp-Rate Control of Photovoltaic Power. *J. Power Sources* **2018**, *384*, 396−407.

(3) Cano, Z. P.; Banham, D.; Ye, S.; Hintennach, A.; Lu, J.; Fowler, M.; Chen, Z. Batteries and Fuel Cells for Emerging Electric Vehicle Markets. *Nat. Energy* **2018**, *3*, 279−289.

(4) Mizushima, K.; Jones, P. C.; Wiseman, P. J.; Goodenough, J. B. Li_xCoO_2 ($0 < X \leq 1$): A New Cathode Material for Batteries of High Energy Density. *Mater. Res. Bull.* **1980**, *15*, 783−789.

(5) Nitta, N.; Wu, F.; Lee, J. T.; Yushin, G. Li-Ion Battery Materials: Present and Future. *Mater. Today* **2015**, *18*, 252−264.

(6) Eftekhari, A. Lithium-Ion Batteries with High Rate Capabilities. *ACS Sustainable Chem. Eng.* **2017**, *5*, 2799−2816.

(7) Su, X.; Wu, Q.; Zhan, X.; Wu, J.; Wei, S.; Guo, Z. Advanced Titania Nanostructures and Composites for Lithium Ion Battery. *J. Mater. Sci.* **2012**, *47*, 2519−2534.

(8) Wagemaker, M.; Kearley, G. J.; van Well, A. A.; Mutka, H.; Mulder, F. M. Multiple Li Positions inside Oxygen Octahedra in Lithiated TiO_2 Anatase. *J. Am. Chem. Soc.* **2003**, *125*, 840−848.

(9) Liu, Q.; Du, C.; Shen, B.; Zuo, P.; Cheng, X.; Ma, Y.; Yin, G.; Gao, Y. Understanding Undesirable Anode Lithium Plating Issues in Lithium-Ion Batteries. *RSC Adv.* **2016**, *6*, 88683−88700.

(10) Earle, M. D. The Electrical Conductivity of Titanium Dioxide. *Phys. Rev.* **1942**, *61*, 56−62.

(11) Rhee, O.; Lee, G.; Choi, J. Highly Ordered TiO_2 Microcones with High Rate Performance for Enhanced Lithium-Ion Storage. *ACS Appl. Mater. Interfaces* **2016**, *8*, 14558−14563.

(12) Lin, Y.-M.; Abel, P. R.; Flaherty, D. W.; Wu, J.; Stevenson, K. J.; Heller, A.; Mullins, C. B. Morphology Dependence of the Lithium Storage Capability and Rate Performance of Amorphous TiO_2 Electrodes. *J. Phys. Chem. C* **2011**, *115*, 2585−2591.

(13) Cao, F.-F.; Guo, Y.-G.; Zheng, S.-F.; Wu, X.-L.; Jiang, L.-Y.; Bi, R.-R.; Wan, L.-J.; Maier, J. Symbiotic Coaxial Nanocables: Facile Synthesis and an Efficient and Elegant Morphological Solution to the Lithium Storage Problem. *Chem. Mater.* **2010**, *22*, 1908−1914.

(14) Cao, F.-F.; Guo, Y.-G.; Wan, L.-J. Better Lithium-Ion Batteries with Nanocable-Like Electrode Materials. *Energy Environ. Sci.* **2011**, *4*, 1634−1642.

(15) Wang, P.; Zhang, G.; Cheng, J.; You, Y.; Li, Y.-K.; Ding, C.; Gu, J.-J.; Zheng, X.-S.; Zhang, C.-F.; Cao, F.-F. Facile Synthesis of Carbon-Coated Spinel $Li_4Ti_5O_{12}$/Rutile-TiO_2 Composites as an Improved Anode Material in Full Lithium-Ion Batteries with $LiFePO_4$@N-Doped Carbon Cathode. *ACS Appl. Mater. Interfaces* **2017**, *9*, 6138−6143.

(16) Zhu, K.; Wang, Q.; Kim, J.-H.; Pesaran, A. A.; Frank, A. J. Pseudocapacitive Lithium-Ion Storage in Oriented Anatase TiO_2 Nanotube Arrays. *J. Phys. Chem. C* **2012**, *116*, 11895−11899.

(17) Kim, J.-H.; Zhu, K.; Kim, J. Y.; Frank, A. J. Tailoring Oriented TiO_2 Nanotube Morphology for Improved Li Storage Kinetics. *Electrochim. Acta* **2013**, *88*, 123−128.

(18) Hibino, M.; Abe, K.; Mochizuki, M.; Miyayama, M. Amorphous Titanium Oxide Electrode for High-Rate Discharge and Charge. *J. Power Sources* **2004**, *126*, 139−143.

(19) Fang, H. T.; Liu, M.; Wang, D. W.; Sun, T.; Guan, D. S.; Li, F.; Zhou, J.; Sham, T. K.; Cheng, H. M. Comparison of the Rate Capability of Nanostructured Amorphous and Anatase TiO_2 for Lithium Insertion Using Anodic TiO_2 Nanotube Arrays. *Nanotechnology* **2009**, *20*, No. 225701.

(20) Borghols, W. J. H.; Lützenkirchen-Hecht, D.; Haake, U.; Chan, W.; Lafont, U.; Kelder, E. M.; van Eck, E. R. H.; Kentgens, A. P. M.; Mulder, F. M.; Wagemaker, M. Lithium Storage in Amorphous TiO_2 Nanoparticles. *J. Electrochem. Soc.* **2010**, *157*, A582−A588.

(21) Xiong, H.; Slater, M. D.; Balasubramanian, M.; Johnson, C. S.; Rajh, T. Amorphous TiO2 Nanotube Anode for Rechargeable Sodium Ion Batteries. *J. Phys. Chem. Lett.* **2011**, *2*, 2560−2565.

(22) Lindström, H.; Södergren, S.; Solbrand, A.; Rensmo, H.; Hjelm, J.; Hagfeldt, A.; Lindquist, S.-E. Li+ Ion Insertion in TiO_2 (Anatase). 2. Voltammetry on Nanoporous Films. *J. Phys. Chem. B* **1997**, *101*, 7717−7722.

(23) Wang, J.; Polleux, J.; Lim, J.; Dunn, B. Pseudocapacitive Contributions to Electrochemical Energy Storage in TiO_2 (Anatase) Nanoparticles. *J. Phys. Chem. C* **2007**, *111*, 14925−14931.

DOI: 10.1021/acsami.8b16994
ACS Appl. Mater. Interfaces 2018, 10, 42513−42523

(24) Xiong, H.; Yildirim, H.; Shevchenko, E. V.; Prakapenka, V. B.; Koo, B.; Slater, M. D.; Balasubramanian, M.; Sankaranarayanan, S. K. R. S.; Greeley, J. P.; Tepavcevic, S.; Dimitrijevic, N. M.; Podsiadlo, P.; Johnson, C. S.; Rajh, T. Self-Improving Anode for Lithium-Ion Batteries Based on Amorphous to Cubic Phase Transition in TiO_2 Nanotubes. *J. Phys. Chem. C* **2012**, *116*, 3181−3187.
(25) Han, J.; Hirata, A.; Du, J.; Ito, Y.; Fujita, T.; Kohara, S.; Ina, T.; Chen, M. Intercalation Pseudocapacitance of Amorphous Titanium Dioxide@Nanoporous Graphene for High-Rate and Large-Capacity Energy Storage. *Nano Energy* **2018**, *49*, 354−362.
(26) Sheppard, A.; Latham, S.; Middleton, J.; Kingston, A.; Myers, G.; Varslot, T.; Fogden, A.; Sawkins, T.; Cruikshank, R.; Saadatfar, M.; Francois, N.; Arns, C.; Senden, T. Techniques in Helical Scanning, Dynamic Imaging and Image Segmentation for Improved Quantitative Analysis with X-Ray Micro-CT. *Nucl. Instrum. Methods Phys. Res., Sect. B* **2014**, *324*, 49−56.
(27) Arns, J.-Y.; Sheppard, A.; Arns, C.; Knackstedt, M.; Yelkhovsky, A.; Pinczewski, W. In *Pore-Level Validation of Representative Pore Networks Obtained from Micro-Ct Images*, Proceedings of the International Symposium of the Society of Core Analysts, 2007; pp 1−12.
(28) Arns, C. H.; Knackstedt, M. A.; Mecke, K. 3d Structural Analysis: Sensitivity of Minkowski Functionals. *J. Microsc.* **2010**, *240*, 181−196.
(29) Steiner, D.; Auer, A.; Portenkirchner, E.; Kunze-Liebhäuser, J. The Role of Surface Films During Lithiation of Amorphous and Anatase TiO_2 Nanotubes. *J. Electroanal. Chem.* **2018**, *812*, 166−173.
(30) Weppner, W.; Huggins, R. A. Electrochemical Methods for Determining Kinetic Properties of Solids. *Annu. Rev. Mater. Sci.* **1978**, *8*, 269−311.
(31) Wen, C. J.; Boukamp, B. A.; Huggins, R. A.; Weppner, W. Thermodynamic and Mass Transport Properties of "LiAl". *J. Electrochem. Soc.* **1979**, *126*, 2258−2266.
(32) Liu, T. C.; Pell, W. G.; Conway, B. E.; Roberson, S. L. Behavior of Molybdenum Nitrides as Materials for Electrochemical Capacitors: Comparison with Ruthenium Oxide. *J. Electrochem. Soc.* **1998**, *145*, 1882−1888.
(33) Levi, M. D.; Aurbach, D. Diffusion Coefficients of Lithium Ions During Intercalation into Graphite Derived from the Simultaneous Measurements and Modeling of Electrochemical Impedance and Potentiostatic Intermittent Titration Characteristics of Thin Graphite Electrodes. *J. Phys. Chem. B* **1997**, *101*, 4641−4647.
(34) Montella, C. Discussion of the Potential Step Method for the Determination of the Diffusion Coefficients of Guest Species in Host Materials: Part I. Influence of Charge Transfer Kinetics and Ohmic Potential Drop. *J. Electroanal. Chem.* **2002**, *518*, 61−83.
(35) Nikitina, V. A.; Fedotov, S. S.; Yu. Vassiliev, S.; Sh. Samarin, A.; Khasanova, N. R.; Antipov, E. V. Transport and Kinetic Aspects of Alkali Metal Ions Intercalation into $AVPO_4F$ Framework. *J. Electrochem. Soc.* **2017**, *164*, A6373−A6380.
(36) Capiglia, C.; Saito, Y.; Kageyama, H.; Mustarelli, P.; Iwamoto, T.; Tabuchi, T.; Tukamoto, H. ^{7}Li and ^{19}F Diffusion Coefficients and Thermal Properties of Non-Aqueous Electrolyte Solutions for Rechargeable Lithium Batteries. *J. Power Sources* **1999**, *81−82*, 859−862.
(37) Valøen, L. O.; Reimers, J. N. Transport Properties of $LiPF_6$-Based Li-Ion Battery Electrolytes. *J. Electrochem. Soc.* **2005**, *152*, A882−A891.
(38) Wang, D.-W.; Fang, H.-T.; Li, F.; Chen, Z.-G.; Zhong, Q.-S.; Lu, G. Q.; Cheng, H.-M. Aligned Titania Nanotubes as an Intercalation Anode Material for Hybrid Electrochemical Energy Storage. *Adv. Funct. Mater.* **2008**, *18*, 3787−3793.
(39) Madian, M.; Giebeler, L.; Klose, M.; Jaumann, T.; Uhlemann, M.; Gebert, A.; Oswald, S.; Ismail, N.; Eychmüller, A.; Eckert, J. Self-Organized TiO_2/CoO Nanotubes as Potential Anode Materials for Lithium Ion Batteries. *ACS Sustainable Chem. Eng.* **2015**, *3*, 909−919.
(40) Madian, M.; Klose, M.; Jaumann, T.; Gebert, A.; Oswald, S.; Ismail, N.; Eychmuller, A.; Eckert, J.; Giebeler, L. Anodically Fabricated TiO_2-SnO_2 Nanotubes and Their Application in Lithium Ion Batteries. *J. Mater. Chem. A* **2016**, *4*, 5542−5552.
(41) Bi, Z.; Paranthaman, M. P.; Menchhofer, P. A.; Dehoff, R. R.; Bridges, C. A.; Chi, M.; Guo, B.; Sun, X.-G.; Dai, S. Self-Organized Amorphous TiO_2 Nanotube Arrays on Porous Ti Foam for Rechargeable Lithium and Sodium Ion Batteries. *J. Power Sources* **2013**, *222*, 461−466.
(42) Jiang, C.; Wei, M.; Qi, Z.; Kudo, T.; Honma, I.; Zhou, H. Particle Size Dependence of the Lithium Storage Capability and High Rate Performance of Nanocrystalline Anatase TiO_2 Electrode. *J. Power Sources* **2007**, *166*, 239−243.
(43) Wagemaker, M.; Borghols, W. J. H.; Mulder, F. M. Large Impact of Particle Size on Insertion Reactions. A Case for Anatase Li_xTiO_2. *J. Am. Chem. Soc.* **2007**, *129*, 4323−4327.
(44) Auer, A.; Portenkirchner, E.; Götsch, T.; Valero-Vidal, C.; Penner, S.; Kunze-Liebhäuser, J. Preferentially Oriented TiO_2 Nanotubes as Anode Material for Li-Ion Batteries: Insight into Li-Ion Storage and Lithiation Kinetics. *ACS Appl. Mater. Interfaces* **2017**, *9*, 36828−36836.
(45) Borghols, W. J. H.; Lutzenkirchen-Hecht, D.; Haake, U.; van Eck, E. R. H.; Mulder, F. M.; Wagemaker, M. The Electronic Structure and Ionic Diffusion of Nanoscale $LiTiO_2$ Anatase. *Phys. Chem. Chem. Phys.* **2009**, *11*, 5742−5748.
(46) Béguin, F.; Frackowiak, E. *Supercapacitors: Materials, Systems, and Applications*; Wiley-VCH Verlag GmbH: Weinheim, Germany, 2013.
(47) Ortiz, G. F.; Hanzu, I.; Djenizian, T.; Lavela, P.; Tirado, J. L.; Knauth, P. Alternative Li-Ion Battery Electrode Based on Self-Organized Titania Nanotubes. *Chem. Mater.* **2009**, *21*, 63−67.
(48) Wu, Q. L.; Li, J.; Deshpande, R. D.; Subramanian, N.; Rankin, S. E.; Yang, F.; Cheng, Y.-T. Aligned TiO_2 Nanotube Arrays as Durable Lithium-Ion Battery Negative Electrodes. *J. Phys. Chem. C* **2012**, *116*, 18669−18677.
(49) Ratajczak, P.; Suss, M. E.; Kaasik, F.; Béguin, F. Carbon Electrodes for Capacitive Technologies. *Energy Storage Mater.* **2019**, *16*, 126−145.
(50) Augustyn, V.; Simon, P.; Dunn, B. Pseudocapacitive Oxide Materials for High-Rate Electrochemical Energy Storage. *Energy Environ. Sci.* **2014**, *7*, 1597−1614.
(51) Brezesinski, K.; Wang, J.; Haetge, J.; Reitz, C.; Steinmueller, S. O.; Tolbert, S. H.; Smarsly, B. M.; Dunn, B.; Brezesinski, T. Pseudocapacitive Contributions to Charge Storage in Highly Ordered Mesoporous Group V Transition Metal Oxides with Iso-Oriented Layered Nanocrystalline Domains. *J. Am. Chem. Soc.* **2010**, *132*, 6982−6990.
(52) Augustyn, V.; Come, J.; Lowe, M. A.; Kim, J. W.; Taberna, P.-L.; Tolbert, S. H.; Abruña, H. D.; Simon, P.; Dunn, B. High-Rate Electrochemical Energy Storage through Li+ Intercalation Pseudocapacitance. *Nat. Mater.* **2013**, *12*, 518.
(53) Ranjusha, R.; Ramakrishna, S.; Nair, A. S.; Anjali, P.; Vineeth, S.; Sonia, T. S.; Sivakumar, N.; Subramanian, K. R. V.; Nair, S. V.; Balakrishnan, A. Fabrication and Performance Evaluation of Button Cell Supercapacitors Based on MnO_2 Nanowire/Carbon Nanobead Electrodes. *RSC Adv.* **2013**, *3*, 17492−17499.
(54) López, M. C.; Ortiz, G. F.; Lavela, P.; Alcántara, R.; Tirado, J. L. Improved Energy Storage Solution Based on Hybrid Oxide Materials. *ACS Sustainable Chem. Eng.* **2013**, *1*, 46−56.
(55) Hemalatha, K.; Prakash, A. S.; K, G.; Jayakumar, M. TiO_2 Coated Carbon Nanotubes for Electrochemical Energy Storage. *J. Mater. Chem. A* **2014**, *2*, 1757−1766.
(56) Opitz, M.; Yue, J.; Wallauer, J.; Smarsly, B.; Roling, B. Mechanisms of Charge Storage in Nanoparticulate TiO_2 and $Li_4Ti_5O_{12}$ Anodes: New Insights from Scan Rate-Dependent Cyclic Voltammetry. *Electrochim. Acta* **2015**, *168*, 125−132.
(57) Brezesinski, T.; Wang, J.; Tolbert, S. H.; Dunn, B. Ordered Mesoporous A-MoO_3 with Iso-Oriented Nanocrystalline Walls for Thin-Film Pseudocapacitors. *Nat. Mater.* **2010**, *9*, 146.

DOI: 10.1021/acsami.8b16994
ACS Appl. Mater. Interfaces 2018, 10, 42513−42523

(58) Ji, H.; Zhao, X.; Qiao, Z.; Jung, J.; Zhu, Y.; Lu, Y.; Zhang, L. L.; MacDonald, A. H.; Ruoff, R. S. Capacitance of Carbon-Based Electrical Double-Layer Capacitors. *Nat. Commun.* **2014**, *5*, No. 3317.
(59) Lindström, H.; Södergren, S.; Solbrand, A.; Rensmo, H.; Hjelm, J.; Hagfeldt, A.; Lindquist, S.-E. Li+ Ion Insertion in TiO_2 (Anatase). 1. Chronoamperometry on CVD Films and Nanoporous Films. *J. Phys. Chem. B* **1997**, *101*, 7710−7716.
(60) Zec, N.; Cvjetićanin, N.; Bešter-Rogač, M.; Vraneš, M.; Gadžurić, S. Electrochemical Performance of Anatase TiO_2 Nanotube Arrays Electrode in Ionic Liquid Based Electrolyte for Lithium Ion Batteries. *J. Electrochem. Soc.* **2017**, *164*, H5100−H5107.
(61) Elliott, S. R. *Physics of Amorphous Materials*; Longman: London, 1990; pp 1238−.
(62) Bai, P.; Bazant, M. Z. Charge Transfer Kinetics at the Solid−Solid Interface in Porous Electrodes. *Nat. Commun.* **2014**, *5*, No. 3585.
(63) Ravet, N.; Chouinard, Y.; Magnan, J. F.; Besner, S.; Gauthier, M.; Armand, M. Electroactivity of Natural and Synthetic Triphylite. *J. Power Sources* **2001**, *97*−*98*, 503−507.
(64) Yamada, H.; Bandaru, P. R. Electrochemical Kinetics and Dimensional Considerations, at the Nanoscale. *AIP Adv.* **2016**, *6*, No. 065325.
(65) Orazem, M. E.; Tribollet, B. *Electrochemical Impedance Spectrosocopy*; John Wiley & Sons: Hoboken, NJ, 2008.
(66) Hirschorn, B.; Orazem, M. E.; Tribollet, B.; Vivier, V.; Frateur, I.; Musiani, M. Constant-Phase-Element Behavior Caused by Resistivity Distributions in Films: I. Theory. *J. Electrochem. Soc.* **2010**, *157*, C452−C457.
(67) Levi, M. D.; Aurbach, D. Simultaneous Measurements and Modeling of the Electrochemical Impedance and the Cyclic Voltammetric Characteristics of Graphite Electrodes Doped with Lithium. *J. Phys. Chem. B* **1997**, *101*, 4630−4640.
(68) Levi, M. D.; Aurbach, D. Frumkin Intercalation Isotherm — a Tool for the Description of Lithium Insertion into Host Materials: A Review. *Electrochim. Acta* **1999**, *45*, 167−185.
(69) Macdonald, J. R.; Kenan, W. R. *Impedance Spectroscopy: Emphasizing Solid Materials and Systems*; Wiley: New York, 1987.
(70) Kang, B.; Ceder, G. Battery Materials for Ultrafast Charging and Discharging. *Nature* **2009**, *458*, 190.

DOI: 10.1021/acsami.8b16994
ACS Appl. Mater. Interfaces 2018, 10, 42513−42523